Canadian Geotechnical Journal

Research Article

Experimental investigation on the water migration and deformation of widely graded coarse soil under drying–wetting cycles

Hongfen Zhao[a,b], **Jiaxi Lu**[a], **Stefano Muraro**[c], **Xu Li**[d], **and Qiming Xiang**[a]

[a]School of Civil Engineering, Sun Yat-sen University, Zhuhai 519082, China; [b]Guangdong Key Laboratory of Marine Civil Engineering, Guangzhou 510275, China; [c]Department of Geoscience and Engineering, Delft University of Technology, 2628, CN, Delft, the Netherlands; [d]Key Laboratory of Urban Underground Engineering of Ministry of Education, Beijing Jiaotong University, Beijing 100044, China

Corresponding author: **Hongfen Zhao** (email: zhaohf7@mail.sysu.edu.cn)

Abstract

Widely graded coarse soils are widely distributed in the mountainous regions of China and are extensively utilised in engineering construction. The volume change of these materials upon intense seasonal wetting and drying cycles presents challenges for the long-term performance of the engineering structures. In this study, the water migration and deformation behaviour of widely graded coarse soils are examined over multiple cycles of drying and wetting. Laboratory tests are integrated with nuclear magnetic resonance and scanning electron microscopy. The results demonstrate that capillary and adsorption forces drive the gradual expulsion and absorption of inter-aggregate and intra-aggregate pore water during the drying–wetting cycles. These two mechanisms differentially influence the microstructure and soil water characteristic curve, soil shrinkage curve, and their hysteretic response. The water content corresponding to the transition between these two regimes is influenced by the coarse content of the soil. In the capillary regime, capillary forces generate normal stresses on the soil skeleton, inducing significant volume changes and resulting in a denser soil structure. In the adsorption regime, on the other hand, adsorption forces control the drainage of pore water within the aggregates. This causes the clay aggregates to shrink without significant deformation of the soil skeleton, the latter being influenced by the coarse content. The hysteresis effect is notably more pronounced in the capillary regime.

Key words: pore water migration, retention behaviour, shrinkage response, hysteresis phenomenon, capillarity, adsorption

Résumé

Les sols grossiers à large granulométrie sont largement répandus dans les régions montagneuses de Chine et sont largement utilisés dans les travaux de génie civil. Le changement de volume de ces matériaux lors des cycles saisonniers intenses de mouillage et de séchage pose des défis pour la performance à long terme des structures d'ingénierie. Dans cette étude, le comportement de migration de l'eau et de déformation des sols grossiers à large granulométrie est examiné sur plusieurs cycles de séchage et d'humidification. Les essais en laboratoire sont intégrés à la résonance magnétique nucléaire (RMN) et à la microscopie électronique à balayage (MEB). Les résultats démontrent que les forces capillaires et d'adsorption entraînent l'expulsion et l'absorption progressives de l'eau interstitielle et intra-agrégat au cours des cycles de séchage et d'humidification. Ces deux mécanismes influencent différemment la microstructure ainsi que la courbe caractéristique de l'eau du sol (SWCC), la courbe de retrait du sol (SSC) et leur réponse hystérétique. La teneur en eau correspondant à la transition entre ces deux régimes est influencée par la teneur en éléments grossiers du sol. Dans le régime capillaire, les forces capillaires génèrent des contraintes normales sur le squelette du sol, induisant des changements de volume significatifs et aboutissant à une structure du sol plus dense. Dans le régime d'adsorption, en revanche, les forces d'adsorption contrôlent le drainage de l'eau interstitielle au sein des agrégats. Les agrégats d'argile se rétractent donc sans déformation significative du squelette du sol, ce dernier étant influencé par la teneur en éléments grossiers. L'effet d'hystérésis est nettement plus prononcé dans le régime capillaire.

Mots-clés : migration de l'eau interstitielle, comportement de rétention, réponse au retrait, phénomène d'hystérésis, capillarité, adsorption

Introduction

In the mountainous regions of China, Quaternary loose deposits are widely distributed, consisting of a heterogeneous mixture of gravel, sand, silt, and clay with a broad particle size distribution spanning several orders of magnitude. These deposits are classified as widely graded coarse soils, exhibiting high shear strength and low compressibility, which make them preferred materials for embankment construction and road engineering applications (Wang et al. 2020; Zhao 2022; Liu et al. 2024). However, due to rainfall infiltration, evaporation or fluctuations in water levels, these materials experience repeated wetting and drying cycles, which drive moisture migration within the soil matrix. Fine particles, in particular, are sensitive to moisture changes, exhibiting shrinkage and swelling during the cycles. This process can result in irreversible deformations, altering the soil pore structure and significantly affecting its hydromechanical behaviour (Farulla et al. 2010; Kong et al. 2018; Mu et al. 2022). Therefore, understanding the moisture migration and the resulting deformation response of widely graded coarse soils during wetting and drying cycles is crucial for evaluating their long-term engineering performance under climatic changes.

The soil water characteristic curve (SWCC) and the soil shrinkage curve (SSC) are key aspects for understanding the water retention and deformation properties of soils during drying and wetting (Ng and Pang 2000*a*; Fredlund 2019; Wen et al. 2021). The SWCC is generally divided into three zones based on the air-entry value (AEV) and residual matric suction: boundary effect zone, transition zone, and residual zone. The relative extension of these three zones depends on the soil type and the stress-state of the soils as a result of both mechanical and hydraulic stress history (Ng and Pang 2000*b*; Ng et al. 2024). Similarly, the SSC is categorised into four stages that reflect changes in the soil volume and water loss: structural shrinkage, normal shrinkage, residual shrinkage, and zero shrinkage (Peng and Horn 2013; Leong and Wijaya 2015). Lu (2019) and Lu and Dong (2017) emphasised the distinct physical mechanisms of capillarity and adsorption on the retention and shrinkage behaviour (Nitao and Bear 1996; Tuller et al. 1999; Frydman and Baker 2009; Lu and Dong 2017; Chen and Lu 2018). Capillarity results from the curved air–water interface in soil pores, while adsorption occurs due to the hydration of exchangeable cations on or within soil particles. The boundary between capillary and adsorption regimes varies significantly among soil types.

The micropore structure of soils gives essential information regarding the soil hydro-mechanical characteristics. Techniques such as scanning electron microscopy (SEM) and mercury intrusion porosimetry (MIP) have been employed to investigate soil microstructure (Romero and Simms 2008; Oualmakran et al. 2016; Tang et al. 2023; Zhao 2023) and to establish connection between the features of SWCC including its hysteretic response and pore size distribution (Ng et al. 2016; Zhang et al. 2022; Sadeghi et al. 2024). SEM is effective for analyzing soil surface features in small samples but provides only 2D images and qualitative data on soil microstructure. MIP offers quantitative analysis of a wide range of pore sizes, assuming cylindrical pore geometry, but may have errors due to undetected or nonintruded pores (Ng et al. 2016). In recent years, nondestructive methods such as nuclear magnetic resonance (NMR) have been increasingly adopted in geotechnical engineering to detect the water content and its interaction with solid particles in porous media. Tian et al. (2014) and Zhao et al. (2024*a*, 2024*b*) have employed NMR to analyse the *T*2 relaxation curve of soils, characterising the pore water distribution in unsaturated soils under varying conditions. NMR provides an effective tool for investigating the relationship between water distribution and the hydraulic behaviour of unsaturated soils. However, to the authors' knowledge, the migration of pore water in widely grade coarse soils under multiple wetting–drying cycles has not been thoroughly investigated, nor have its effects on soil microstructure, water retention, and deformation behaviour.

Water migration in the soil has been shown to drive microstructural evolution, which in turn impacts the hydromechanical behaviour. Coarse and fine particles within the soil rearrange into various structures depending on the proportion of coarse particles. As the content of coarse particles varies, soil structure shifts from being fine-controlled to coarse-controlled. In coarse soils, a dual-porosity structure is formed, characterised by both intra-aggregate pores and inter-aggregate pores (Li and Zhang 2009; Zhao et al. 2013*a*). During drying–wetting cycles, the migration and redistribution of pore water in inter-aggregates and intra-aggerates pores within clay aggregates can differentially influence the hydro-mechanical behaviour of widely graded coarse soils. While much of the existing research on microstructure changes during drying–wetting has primarily focused on fine-grained soils (Burton et al. 2015; Sun and Cui 2017; Ma et al. 2020; Zhao 2023), studies on widely graded coarse soils remain limited. The hysteretic behaviour of pore water migration, SWCC, and SSC for these soils under multiple drying–wetting cycles has still not been fully explored.

The objective of this paper is to investigate the pore water migration and deformation response in widely graded coarse soils subjected to multiple drying and wetting cycles. To achieve this, a series of NMR tests, soil shrinkage tests, and soil water retention tests were conducted on widely graded coarse soils with five different coarse contents. Multiple drying–wetting cycles were performed to examine the hysteretic behaviour. Additionally, SEM tests were performed to assess changes in soil fabric due to drying and wetting cycles. Eventually, the migration of pore water during multiple wetting–drying cycles and its effects on microstructural changes, water retention capacity, and deformation response were summarised.

Materials and methods

Tested materials

To investigate the effect of coarse content on the deformation and water migration of widely graded coarse soil under

Fig. 1. Grain-size distribution curves of five types of soils.

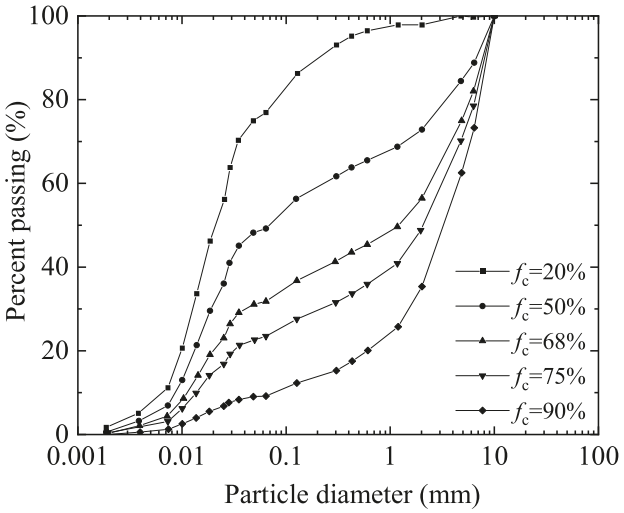

drying–wetting cycles, five types of soil with different coarse contents were mixed from a completely decomposed granitic soil at a construction site in Zhuhai, China. The grain-size distribution curves of the tested material are shown in Fig. 1. The particle size ranges from 0.002 to 10 mm. The mean particle diameter, D_{50}, ranges between 0.015 and 3.5 mm. This range effectively represents widely graded and coarse-grained soils found in the field. The five types of soils have coarse contents, f_c, of 20%, 50%, 68%, 75%, and 90%, respectively. Here, f_c represents the percentage of particles larger than 0.075 mm, as defined by ASTM (2020). The liquid limit, plastic limit, and shrinkage limit of the fine fraction are 47%, 32%, and 8%, respectively. The five types of soil are classified as lean clay with sand (CL), sand lean clay (sandy CL), silty sand with gravel (SM with gravel 1), silty sand with gravel (SM with gravel 2), and well-graded sand with silt and gravel (SW–SM with gravel) according to ASTM D2487 (ASTM 2020). Standard compaction tests using a standard effort of 600 kNm/m^3 were conducted on each soil to obtain the optimal water contents and maximum dry densities. The corresponding optimum water contents for f_c = 20%, 50%, 68%, 75%, and 90% are 20%, 13.5%, 12.5%, 12%, and 10%, with maximum dry densities of 1.55, 1.83, 1.85, 1.9, and 1.95 g/cm^3, respectively. The specific gravity of all soils is $G_s = 2.64$. The specimens were prepared using a moist tamping technique and were statically compacted to the same void ratio of 0.62 at their respective optimum water contents. Chemical and mineral compositions are measured by X-ray diffraction method. The primary mineral in fines is kaolin, followed by montmorillonite, and the rest is white mica and quartz.

Experimental program

Retention tests were conducted to characterize the water retention behaviour during multiple drying–wetting cycles, while shrinkage tests focused on assessing volume changes. To investigate the water migration and microstructural evolution during the drying–wetting process, low-frequency NMR, and SEM tests were conducted on samples with different moisture contents at various stages of the drying–wetting cycles.

To ensure that all tests follow the same suction path, the prepared samples were first saturated under vacuum conditions. The pressure plate (i.e., suction up to 1400 kPa) and WP4C Dew Point (i.e., suction greater than 1400 kPa) are combined to derive the SWCC over the entire suction range. In the pressure plate test, air pressure is incrementally increased or decreased according to the specified suction path. The volume of water drained or absorbed by the soil is measured once the water content stabilises, defined as a total change in soil mass of no more than 0.01% over 24 h, meeting the moisture equilibrium criteria for suctions greater than 1000 kPa (Li 2023). Although the SWCC is affected by the applied net stress (Ng et al. 2024), in this study, no vertical load was applied during the pressure plate tests. Shrinkage tests were conducted on samples with a height and diameter of 61.8 mm. The samples were placed on a balance and allowed to dry and wet slowly in a climate-controlled room maintained at 20 °C with 60% relative humidity. The SSC was determined by analysing the relationship between void ratio and water content. Saturated samples were subjected to multiple drying stages. During the drying process, samples were dried to a target moisture content, and then sealed with a beaker to equilibrate at a constant moisture level for 48 h before mass and dimension measurements were taken. Following the drying stage, the wetting process began. Wetting was achieved by spraying a specific amount of water onto the sample surface and then sealing it with a beaker for 48 h to reach equilibrium. A total of five drying and wetting cycles were conducted. At each stage, the sample mass was recorded using a balance with 0.01 g accuracy. The sample volume was calculated by measuring the height and diameter with a calliper. Measurements were taken at five different positions, and the average was used. After the tests, samples were oven-dried at 105 °C to determine the initial and the current water content. NMR tests were performed using a low-field NMR analyser to investigate water migration during drying–wetting cycles. The analyser features a permanent magnetic field strength of 0.5 Tesla, with the magnet temperature maintained at 32 ± 0.01 °C to ensure a stable and uniform magnetic field. A 60 mm diameter probe was used. Specimens with varying water contents (i.e., saturated, 24%, 19%, 16%, 13%, 11%, 9%, 7%, 5%, air-dried) from different stages of drying and wetting cycles were placed in the NMR apparatus to measure T_2 spectra. SEM analysis was performed to examine the surface structure of samples. Saturated specimens were cut into several pieces, which were then dried and wetted for different durations to achieve specific target water contents. Once a piece reached its target water content, it was equilibrated for 48 h. For SEM tests, samples were first fast freeze-dried with liquid nitrogen to remove water while preserving the structure, followed by 24 h in a vacuum chamber at temperatures below −57 °C for water sublimation. The dehydrated samples were then gold-coated. SEM imaging analyses at different magnification levels were conducted to visualise the samples surface structure.

Fig. 2. Photos of five soils: (*a*) f_c = 20%; (*b*) f_c = 50%; (*c*) f_c = 68%; (*d*) f_c = 75%; and (*e*) f_c = 90%.

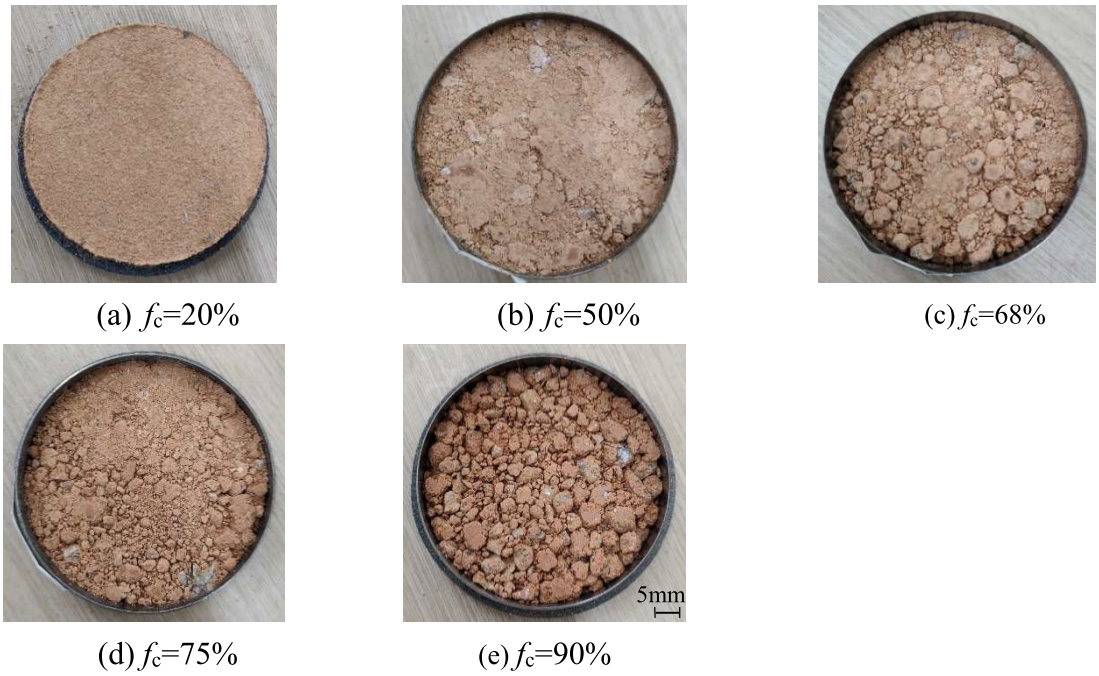

Test results

Soil structure of widely graded coarse soils

As shown in Fig. 2, coarse and fine grains rearrange into different packings based on the coarse content. The composition of the skeleton for the five types of compacted specimens (f_c = 20%, 50%, 68%, 75%, and 90%) gradually shifts from clay aggregates to coarse particles. Research by Li and Zhang (2009) on the microporosity of coarse granular soils with the same particle size distributions identified 70% coarse content as the critical threshold between coarse-controlled and fines-controlled structures. Soils with coarse contents of 20% and 50% are considered fine-controlled, where clay aggregates form the skeleton, and larger particles are embedded within the clay matrix (Zhao et al. 2013*a*). Transition soils, with coarse contents of 68% and 75%, are influenced by both clay aggregates and coarse particles. In soils with 90% coarse content, grain-to-grain contacts among coarse particles form the primary skeleton, while finer particles fill the inter-particle pores, resulting in a coarse-controlled structure.

Figure 3*a* shows the SEM and schematic microstructures of transition soils with a coarse content of 75%. Soil specimens prepared by static compaction exhibit single clay particles aggregating into clusters, forming larger aggregates. The soil skeleton consists of both clay aggregates and coarse particles, resulting in a dual-porosity structure characterised by inter-aggregate and intra-aggregate pores, as reported by Zhao et al. (2013*b*). The arrangement of single particles in a clay aggregate produces numerous intra-aggregate pores. The water stored in the intra-aggregate pores is referred to as intra-aggregate pore water (see Fig. 3*b*). Clays are mostly made up of layered silicates, and their surfaces are negatively charged because of isomorphic substitution and broken bonds at the edges. As shown in the upper right corner of Fig. 3*b*, this negative charge attracts cations from the surrounding solution, forming the electrical double layer with the stern layer and the diffuse layer. The stern layer consists of cations adsorbed directly onto the clay surface, bound tightly, and immobile. Beyond this, the diffuse layer contains a mix of cations and anions, where ions are more loosely associated and can move more freely. The water in the diffuse layer can be collectively regarded as intra-aggregate pore water. The arrangement of clay aggregates produces inter-aggregate pores. The water stored in the inter-aggregate pores is referred to as inter-aggregate pore water. During the drying–wetting processes, pore water is expelled or absorbed into inter-aggregate and intra-aggregate pores during different stages, which plays a crucial role in soil volume changes.

Based on the previously reported critical coarse content value of 70%, and the cross-sectional images of the soil types in this study, the schematic microstructures of fines-controlled and coarse-controlled soils are schematically illustrated in Fig. 4. For fines-controlled soils (f_c = 20% and f_c = 50%), large particles are dispersed within a clay matrix, with the skeleton primarily formed by densely compacted clay aggregates (Fig. 4*a*). The pore structure is dominated by intra-aggregate pores, with a higher proportion of water adsorbed on the particle surfaces. In contrast, coarse-controlled soils exhibit a skeleton formed by direct grain-to-grain contacts between coarse particles, with finer particles partially filling the larger inter-particle voids (Fig. 4*b*). This results in large inter-particle pores between the coarse particles, while intra-aggregate pores persist within the clay aggregates. In coarse-grained soils, water is primarily present as free water in the large inter-particle pores. Additionally, a small amount

Fig. 3. Microstructure and pore water distribution of $f_c = 75\%$ (transition soil): (*a*) scanning electron microscopy and (*b*) conceptual sketch of pore water distribution.

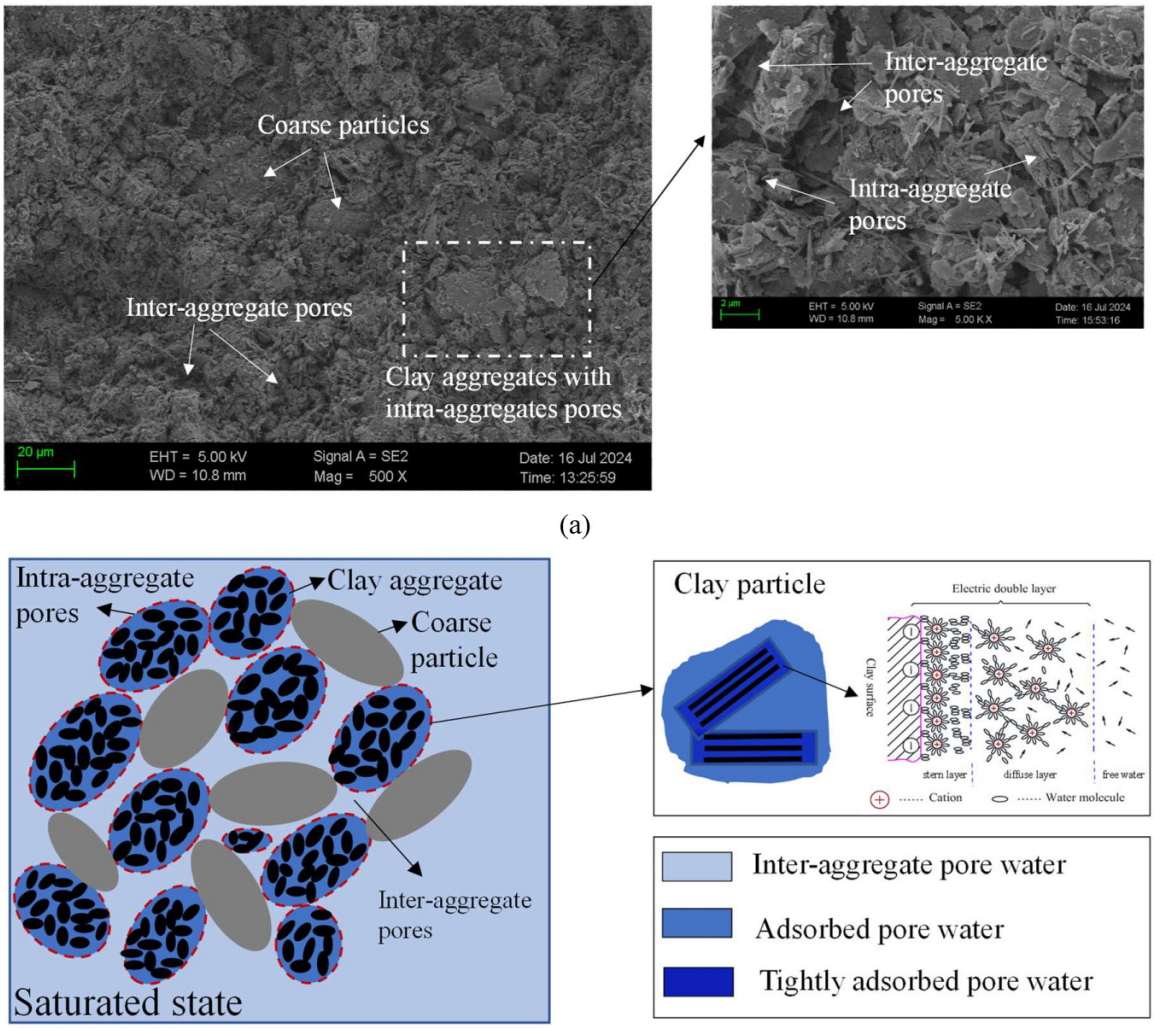

of adsorbed water forms a thin layer around the particle surfaces and within clay aggregates.

Pore water migration during drying and wetting processes

Figure 5 depicts the measurements of the T_2 spectrum at various water contents during the first hydraulic cycle for both wetting and drying paths from NMR. The horizontal axis of the graph represents the T_2 relaxation time, while the vertical axis represents the dimensionless NMR signal amplitude. T_2 value reflects the location of pore water within the sample: water in large pores has a higher T_2 value, while water in small pores and bound water has lower T_2 values. Three characteristic T_2 values are defined as follows: the dominant pore radius (T_{dom}), which corresponds to the first peak value, the maximum water-holding pore radius (T_{max}), representing the maximum pore radius at which the pore water volume is nonzero, and the minimum water-holding pore radius (T_{min}), corresponding to the minimum pore radius. The area under the T_2 curve corresponds to the water content within the corresponding T_2 time range. The T_2 curve of unsaturated soil only represents the pore information of the water-filled part of the soil, rather than the complete pore distribution of the soil. Figure 6 illustrates the variations of the three characteristic T_2 values (T_{dom}, T_{max}, and T_{min}) with water content under the first drying and wetting cycle.

As shown in Fig. 5*a*, for soil with $f_c = 20\%$, the T_2 distribution exhibits a unimodal pattern. During the drying process, as pore water gradually drains, the T_2 distribution curve shifts leftward. As the water content decreases, T_{max} steadily decreases, and T_{dom} and its corresponding amplitude values also reduce. This reveals that during a drying process, pore water initially drains from larger pores (i.e., T_{max} decreases) and subsequently from smaller pores (i.e., T_{min} decreases). If the soil remains undeformed, T_{min} is theoretically unaffected in the initial stages of drainage. However, as pore wa-

Fig. 4. Microstructure of (*a*) fines-controlled soil and (*b*) coarse-controlled soil.

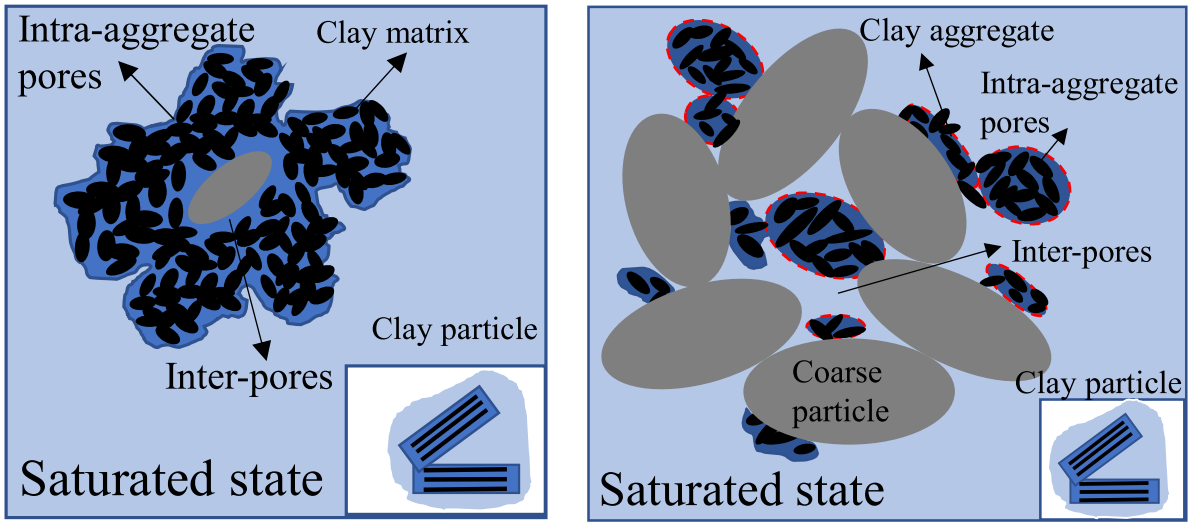

ter is expelled, the T_{min} value progressively decreases, indicating changes in the pore structure throughout the drying process.

As discussed in Zhao et al. (2024*a*), the T_2 curve exhibits a specific threshold value, referred to as the T_2 cutoff value (T_{2c}), which separates the curve into two distinct ranges. When the T_2 value of the pore fluid exceeds this threshold, the fluid is classified as mobile (e.g., capillary water or free water). Conversely, when the T_2 value falls below this threshold, the fluid is confined within the pores (e.g., adsorbed water). As shown in Fig. 5, samples oven-dried at 105 °C do not effectively remove tightly bound water. Consequently, the T_2 distribution of the dried samples shifts toward lower relaxation. For example, for the dried sample with f_c = 20%, the T_2 distribution ranges between 0.008 and 2 ms, with a T_{dom} value of 0.554 ms and a corresponding peak value of 723.4 (Fig. 5*a*). Although T_{max} of the dried sample slightly increases with higher coarse content, for the dried sample with f_c = 90%, T_{max} reaches approximately 2.8 ms. Among all cases, the smallest T_{max} of 2 ms is most likely to represent the boundary between adsorbed water and capillary water in terms of T_2 values.

Li and Zhang (2009) used MIP and SEM techniques to investigate the micropore structure of widely graded coarse soils during drying processes. Their test results revealed the existence of a dual-porosity structure within compacted soil samples, consisting of intra-aggregate pores and inter-aggregate pores. The characteristic pore size (r_c) distinguishing those two types of pores was approximately 1 μm. Based on the pore structure coefficient (C_r = 0.5) suggested by Zhao et al. (2024*a*), the corresponding T_{2c} is determined to be 2 ms, following the theoretical relationship between T_2 relaxation time and pore radius:

$$\frac{1}{T_2} = \frac{C_r}{r_c} \quad (1)$$

where r_c is the equivalent pore radius, and C_r is the pore structure coefficient.

By combining experimental observations from NMR drying tests and theoretical analysis based on pore structure models, 2 ms can be identified as the critical threshold value separating capillary regime and adsorption regime. The corresponding water content at the transition points between the two regimes for four soil types is reported in Table 1.

As shown in Fig. 6, the three characteristic values, T_{dom}, T_{max}, and T_{min}, decrease with the water content along drying, displaying a staged pattern. For f_c = 20%, the water content between the two regimes is about 11%. During the initial drying process of the soil, as air invades the pores, the water–air meniscus forms first in the large inter-pores. In this regime, both capillary and adsorbed water contribute to the overall soil water content. However, during the first part of the drying process, the water exchange is primarily governed by capillarity with suction generated by the curvature of the air–water interface within the inter-aggregate pores. As capillary forces develop, the soil matrix shrinks, leading to a decrease in T_{dom}, T_{max}, and T_{min} with bulk water draining from the soil. In the second stage, physicochemical forces, such as van der Waals interactions and electric double-layer effects, govern the migration of adsorbed water, defining the adsorption regime. Water molecules adhere to or are embedded within soil particles, influenced by the hydration of exchangeable cations, mineral surfaces, or crystal interlayers. Adsorbed water gradually drains from the clay aggregates, causing shrinkage of clay aggregates. The shrinkage of clay aggregates significantly reduces T_{dom}, T_{max}, and especially T_{min} (Fig. 6). For fully dried samples, only tightly adsorbed water remains. When the water content becomes extremely low, T_{min} falls beyond the detection range of the instrument, resulting in a constant value.

The T_2 distribution curves of soil with f_c = 20% along the wetting path are shown in Fig. 5*a*. Contrary to the drying process, during the wetting process, the peak area, the T_{dom},

Fig. 5. T_2 spectrum of soil under first drying and wetting cycle: (*a*) $f_c = 20\%$; (*b*) $f_c = 68\%$; (*c*) $f_c = 75\%$; (*d*) $f_c = 90\%$.

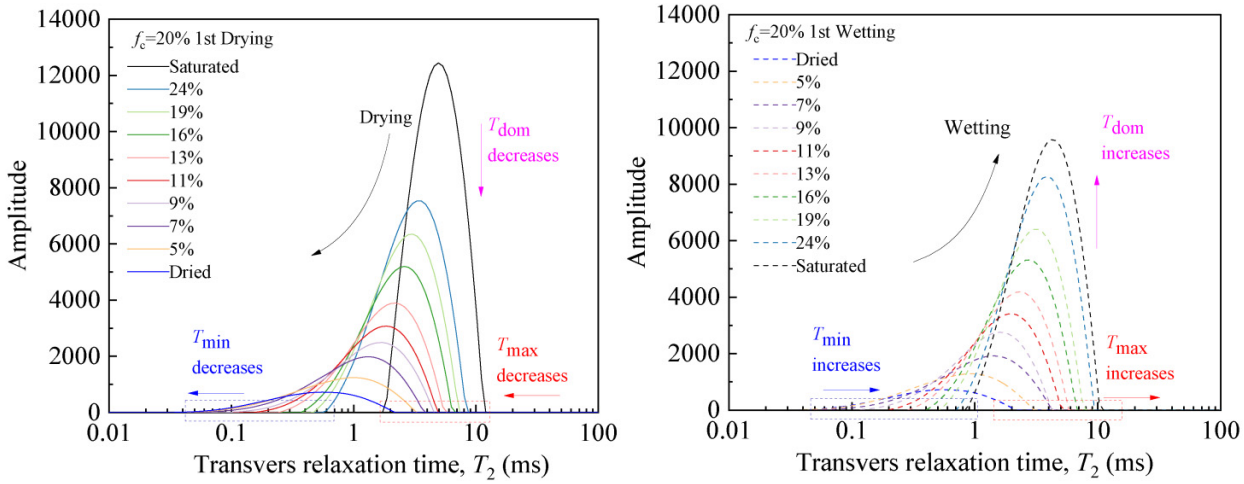

(a) f_c=20%

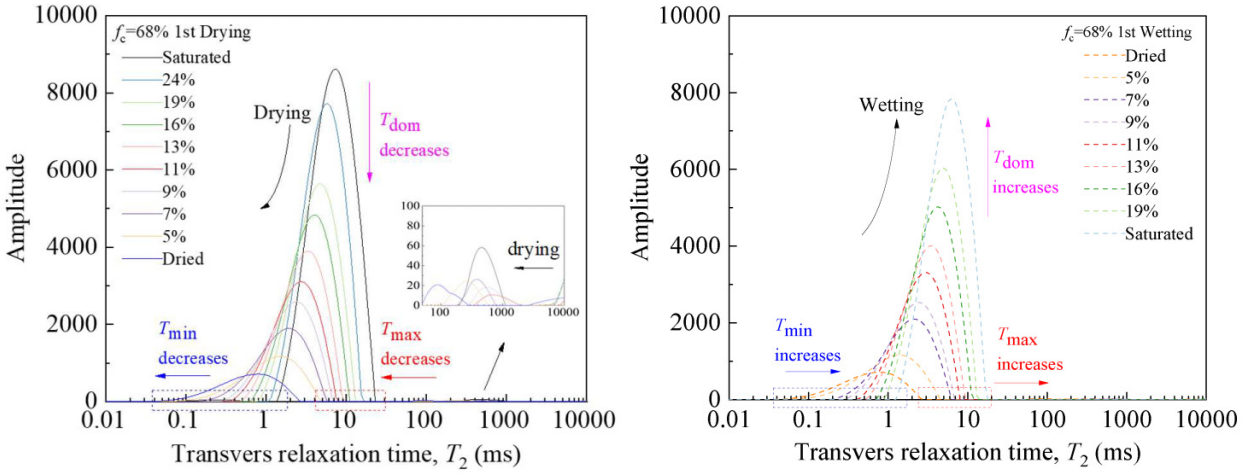

(b) f_c =68%

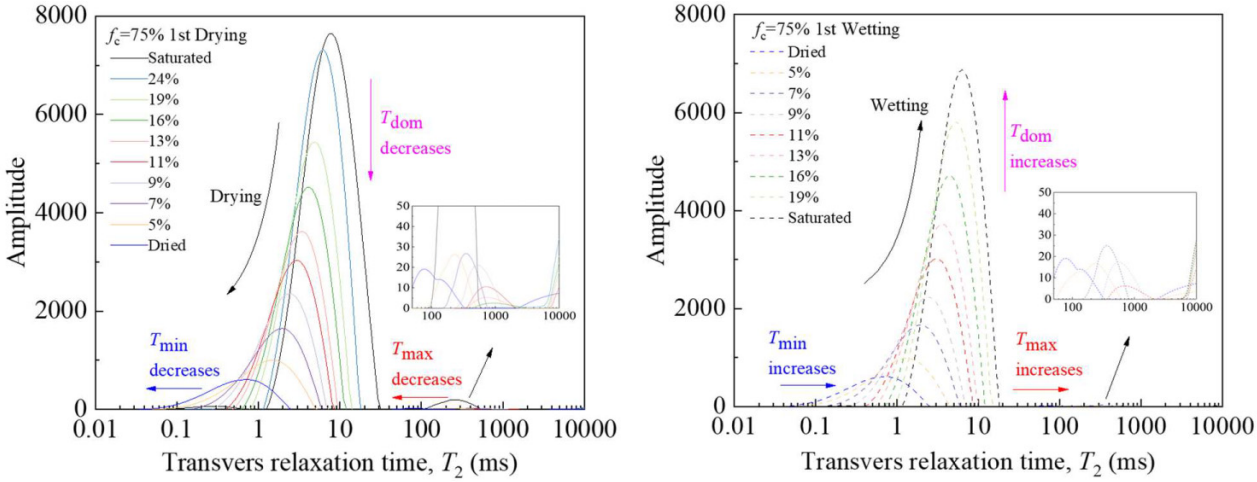

(c) f_c =75%

Fig. 5. (*concluded*).

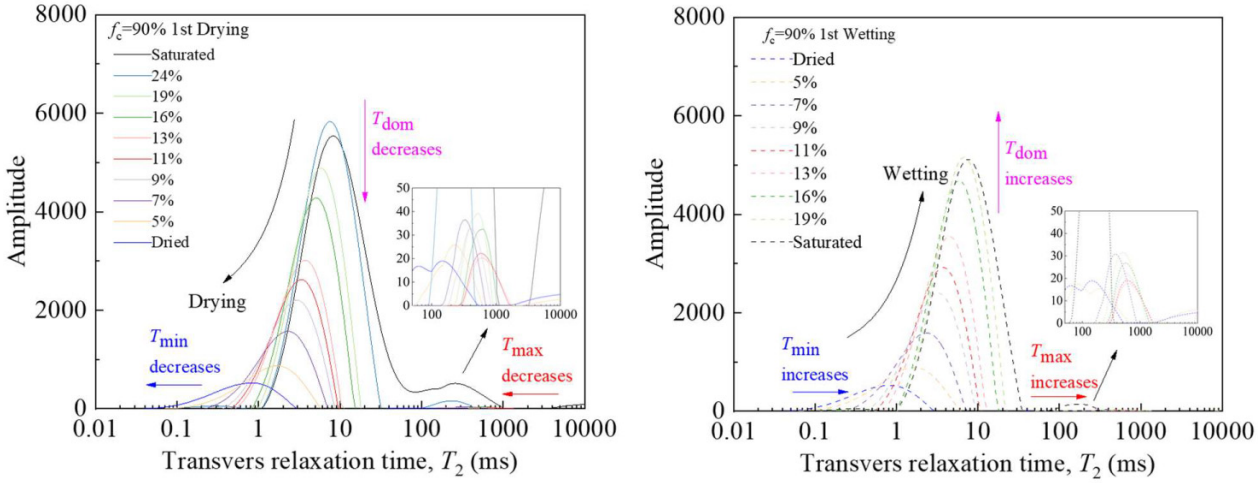

(d) f_c =90%

Fig. 6. Variation of T_{min}, T_{max}, T_{dom} with water content: (*a*) f_c = 20%; (*b*) f_c = 68%; (*c*) f_c = 75%; and (*d*) f_c = 90%.

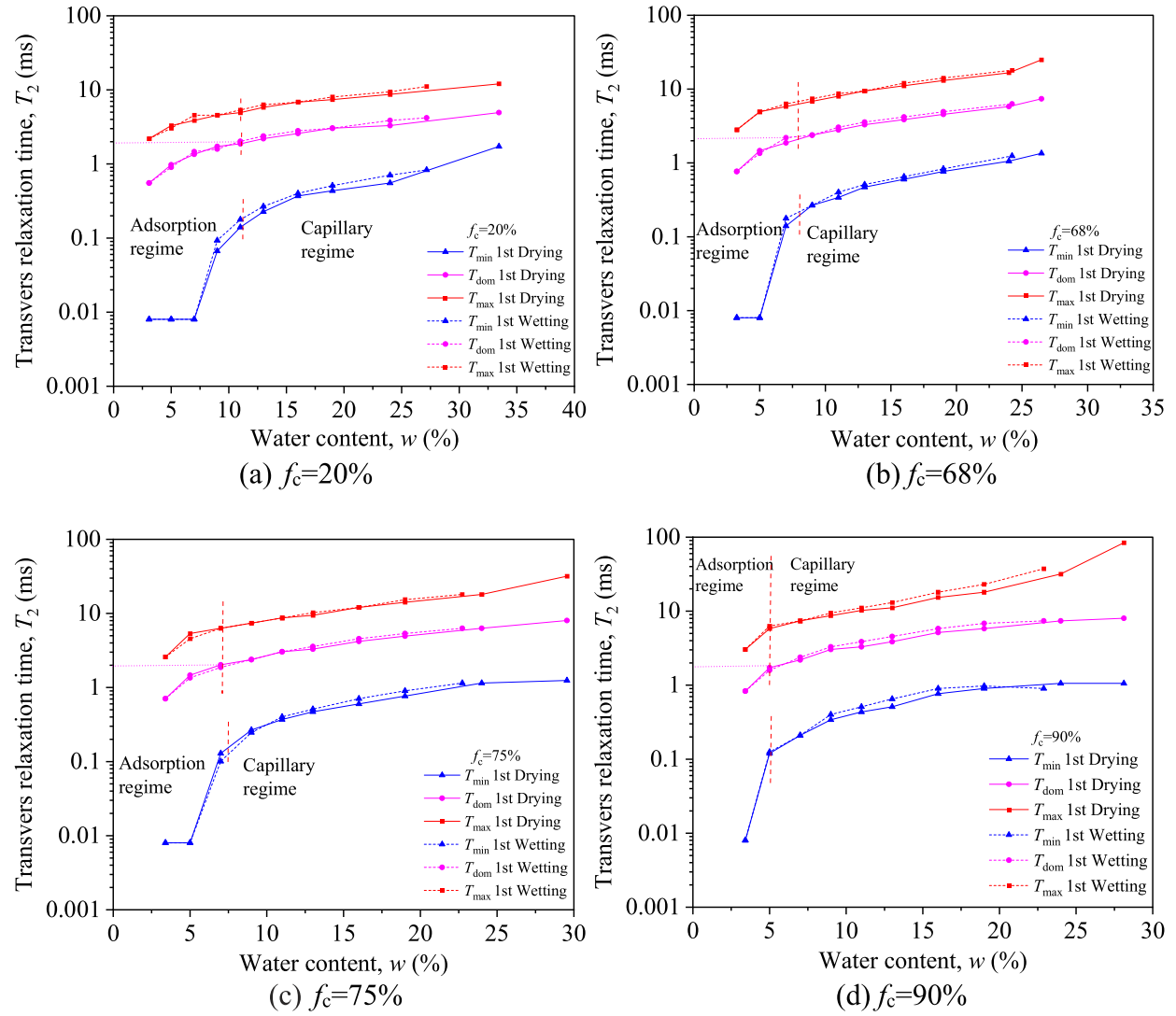

Table 1. Key points in SWCC and SSC at the first drying process.

Specimen	Inflection w of T_2 from NMR (%)	Inflection w of SWCC (%)		Inflection w of SSC (%)
	Transition between capillarity and adsorption regime	AEV	Residual water content	Transition between capillarity and adsorption regime
$f_c = 20\%$	11	32	10	10
$f_c = 68\%$	8	28	8	8
$f_c = 75\%$	7	23	8	8
$f_c = 90\%$	5	22	5	5

Note: SWCC, soil water characteristic curve; SSC, soil shrinkage curve; NMR, nuclear magnetic resonance; AEV, air-entry value.

T_{max}, and T_{min} all increase with the water content. The staged pattern with the transition between capillarity and adsorption regimes identified during the drying process can also be seen for the wetting process. As the soil becomes re-saturated, some air remains trapped in the large pores and forms a contiguous phase with the pore water, leading to a saturated water content after wetting lower than the initial water content.

During the initial stage of wetting in the low water content region, the small interlayer spacing generates strong van der Waals forces. The outermost layer of oxygen and hydroxyl ions at the particle surface attracts hydrogen ions from water molecules. Water is initially adsorbed onto the mineral surfaces of clay aggregates (i.e., kaolinite and montmorillonite). If the external environment contains higher water vapour potential, exchangeable cations can overcome the strong intermolecular forces between the crystal layers, attracting water and causing the crystal structure to expand (Lu and Khorshidi 2015). As a result, T_{min} increases more rapidly than T_{dom} and T_{max} during this stage. As water content increases, water spreads as thin films on particle surfaces and through menisci at particle contacts, eventually filling the inter-aggregate pores as driven by the air–water interface. In this stage, T_{dom}, T_{max}, and T_{min} all gradually increase with water content.

As the coarse content increases, the pores in the soil become larger and more abundant (Figs. 3 and 4). Consequently, the maximum T_2 value on the horizontal axis in Figs. 5*b*-5*c* extends to 10 000 ms. The T_2 distribution in the 100–1000 ms range becomes more prominent, particularly when the coarse content reaches 90%. The two peaks in the distribution correspond to T_{dom} values of 8.02 and 261.3 ms, respectively. This feature is directly related to the soil pore structure. As illustrated in Fig. 4*d*, in coarse-grained soils, water primarily exists as free water within the large inter-particle pores. A thin layer of adsorbed water forms around particle surfaces and within clay aggregates. The primary T_2 distribution range for the saturated soil sample spans from 0.097 to 1035 ms, with a maximum T_{max} significantly higher than that of soil with a coarse content f_c of 20%, which only reaches up to 12.034 ms.

For coarse-controlled soil, water initially drains rapidly from the larger inter-aggregate pores, causing a sharp decrease in T_{max} while T_{min} remains relatively constant (Fig. 6*d*). During the adsorption regime, water drains from the intra-aggregate pores within clay aggregates, causing the clay aggregates to shrink, resulting in a rapid decrease in T_{min}. As shown in Table 1, the threshold T_2 value is influenced by the coarse content. As the coarse content increases from 20% to 90%, the water content at the transition points decreases from 11% to 5%. These results align with findings by Lu and Dong (2017), who showed that the total amount of adsorbed water is linearly related to specific surface area and cation exchange capacity, both of which decrease as the coarse content increases.

A conceptual model of pore water distribution at different states

To assess the soil fabric evolution during pore water migration through drying and wetting cycles, samples were freeze-dried for SEM analyses at different target water contents following drying and wetting paths. Figures 7*a* and 7*b* show the results for $f_c = 20\%$ during the drying and wetting processes, respectively. As illustrated in Fig. 4, the soil skeleton for $f_c = 20\%$ mainly consists of fine-grained particles, with coarse particles dispersed within the fine matrix. Based on the fabric evidence from SEM analysis, a conceptual representation of pore water distribution and fabric rearrangement at different drying and wetting stages is offered in Fig. 8. The fines compacted at the optimum water content usually exist in the form of an aggregated structure. However, it is worth noticing that the initial saturation of the sample was achieved through vacuum saturation under lateral confinement, thus preventing lateral expansion. As a result, the saturated sample displayed a rather homogeneous soil fabric with particles arranged more tightly and uniformly distributed pores as shown in Fig. 7*a* ($w = 30\%$). In this stage, the crystal platelets within the clay aggregates are fully saturated, with larger and more abundant intra-aggregate pores between them (Fig. 8*a*-1). In the capillary domain regime, as water in the inter-aggregate pores drains, air–water interfaces form between the clay aggregates, causing the soil to become unsaturated. On the contrary, the water in the intra-aggregate pores remains largely unaffected, as illustrated in Fig. 8*a*-2. Particles rearrangement caused by drainage of inter-aggregate pore water can be observed in Fig. 7*a* ($w = 20\%$) leading to a denser soil structure.

Based on the transition point of T_2 between the capillarity and adsorption regimes (see Fig. 6 and Table 1), as the water content decreases to around 11%, water migration gradually shifts from the capillary domain to the adsorption domain. This leads to the expulsion of water from the intra-aggregate pores. As the small pores in the clay matrix shrink, soil aggregates begin to form. At water contents between 13% and 9%, these clay aggregates become more

Fig. 7. Impression of fabric change from SEM on sample with $f_c = 20\%$ during: (*a*) drying process and (*b*) wetting process.

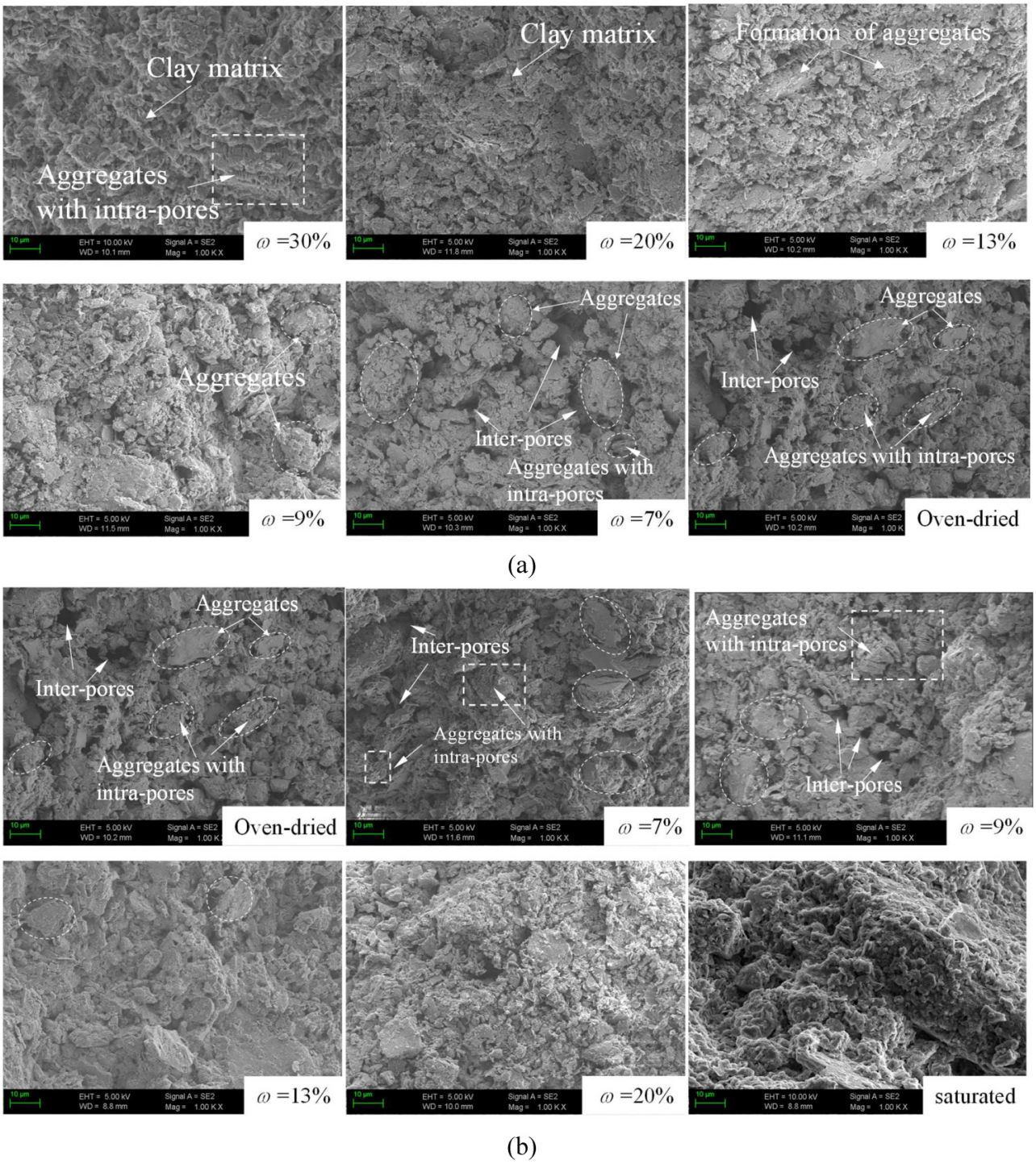

noticeable in the soil matrix (Fig. 7*a*). During this stage, the overall volume change of the soil is minimal, which reduces contacts between the clay aggregates and results in the formation of new inter-aggregate pores (Fig. 7*a*; $w = 7\%$). As illustrated in the conceptual diagram (Fig. 8*a*-4), at this stage, only tightly adsorbed water adheres around the particles under the influence of van der Waals forces, causing the arrangement of the crystal platelets to become more compact.

As shown in Fig. 7*b*, upon wetting under unconfined conditions (i.e., free swelling), at low water contents (7%, 9%, and 13%), clay aggregates absorb water through adsorption and begin to swell. The aggregate particles gradually occupied inter-aggregate pores and increased the contact areas between particles. As the water content continues to rise, larger pores fill with water, reducing surface tension at the air–water interface, and leading to an overall increase in soil volume. Ultimately, at higher water content, the clay

Fig. 8. Conceptual sketch of pore water distribution model: (*a*) fines-controlled soil; (*b*) transition soil; and (*c*) coarse-controlled soil.

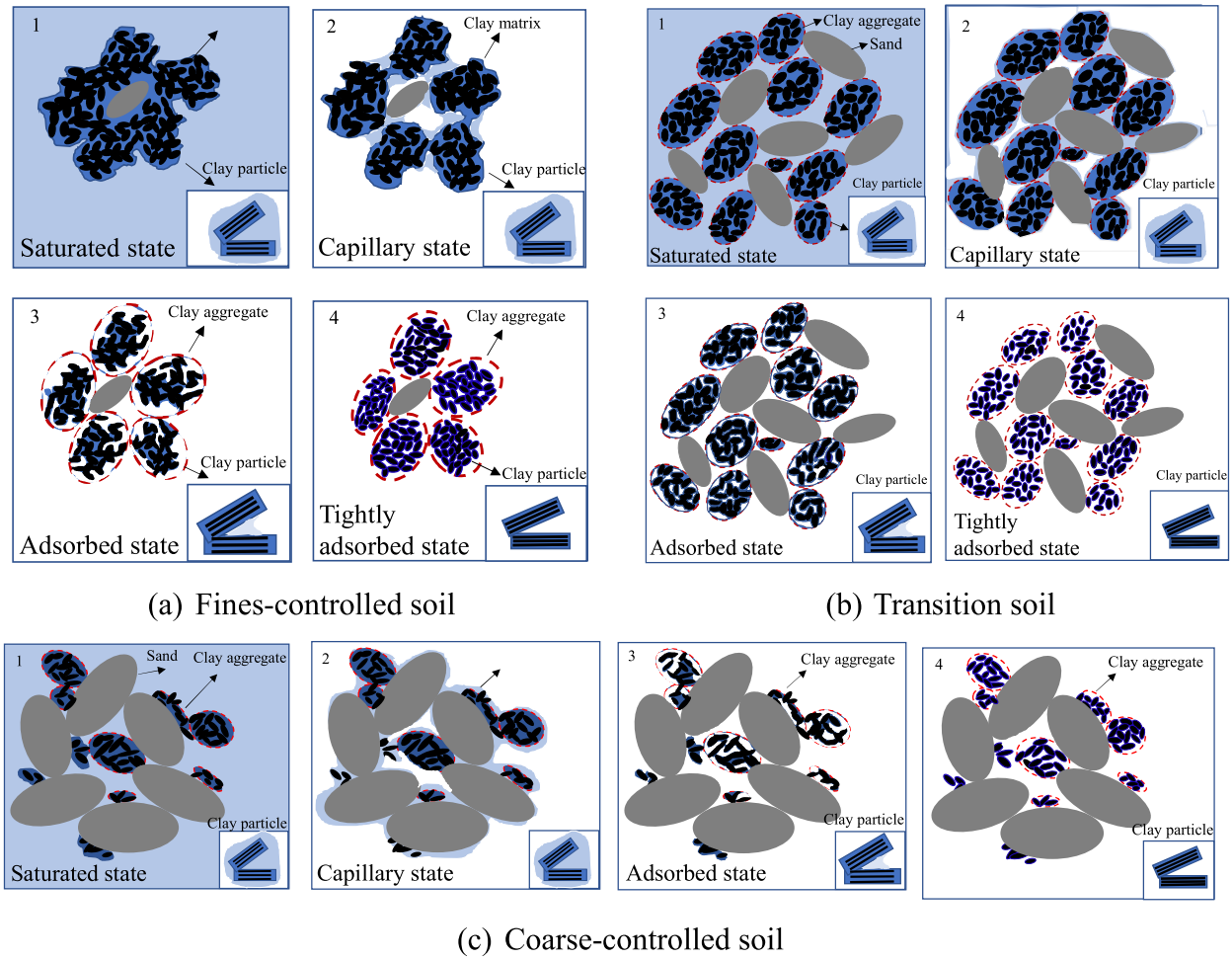

aggregate structure weakens, forming a homogeneous structure. However, the microstructure of the soil typically cannot fully recover during wetting and drying cycles. As shown in Fig. 7*b*, as the soil approaches saturation upon wetting after drying, clay aggregates remain present in contrast to a more uniform fabric observed in the original saturated sample (Fig. 7*a*; $w = 30\%$).

Supported by the NMR results in Figs. 5*b*-5*d*, the corresponding conceptual mechanism of water distribution and fabric rearrangement upon drying for transition soils and coarse-controlled soils are illustrated in Figs. 8*b* and 8*c*. As illustrated in Fig. 8*b*-1, in transition soils, both clay aggregates and coarse particles form the overall soil skeleton. The intra-aggregate pores are primarily located within the clay aggregates, while the inter-aggregate pores exist between the coarse particles and the clay aggregates. In the saturated state, water fills the spaces between the clay aggregates and sand particles. As drying begins capillary forces maintain continuous water films around the clay aggregates and sand particles, causing clay particles to draw closer and resulting in notable volume changes (Fig. 8*b*-2). With further drying, the water films break, leaving only adsorbed water around the clay aggregates and particles, leading to the shrinking of the clay aggregates. In the final stage of drying, as shown in Fig. 8*b*-4, only tightly adsorbed water remains, confined to a thin layer closely adhering to the surface of the clay particles due to van der Waals forces. The shrinkage of clay aggregates weakens the contact between the aggregates themselves and between the aggregates and sand particles. In coarse-controlled soils, the structure is supported by a skeleton of coarse particles. Since coarse particles are more stable than clay aggregates under the influence of water, in coarse-controlled soils the overall structure remains largely unchanged after drying, with shrinkage occurring primarily in the clay aggregates (Fig. 8*c*).

Soil water retention during drying and wetting processes

Based on the microscopic structure evidence, four types of soil were selected to illustrate the impact of the coarse content of the soil water retention behaviour: fines-controlled soils ($f_c = 20\%$), transition-soils ($f_c = 68\%$ and $f_c = 75\%$), and coarse-controlled soils ($f_c = 90\%$).

Figure 9 presents the SWCC for each soil in terms of suction, ψ, and water content, w, during the first drying–wetting cycle. The retention curves for the four types of soil ex-

Fig. 9. Soil water characteristic curves under first drying and wetting cycle: (*a*) $f_c = 20\%$; (*b*) $f_c = 68\%$; (*c*) $f_c = 75\%$; and (*d*) $f_c = 90\%$. AEV, air-entry value.

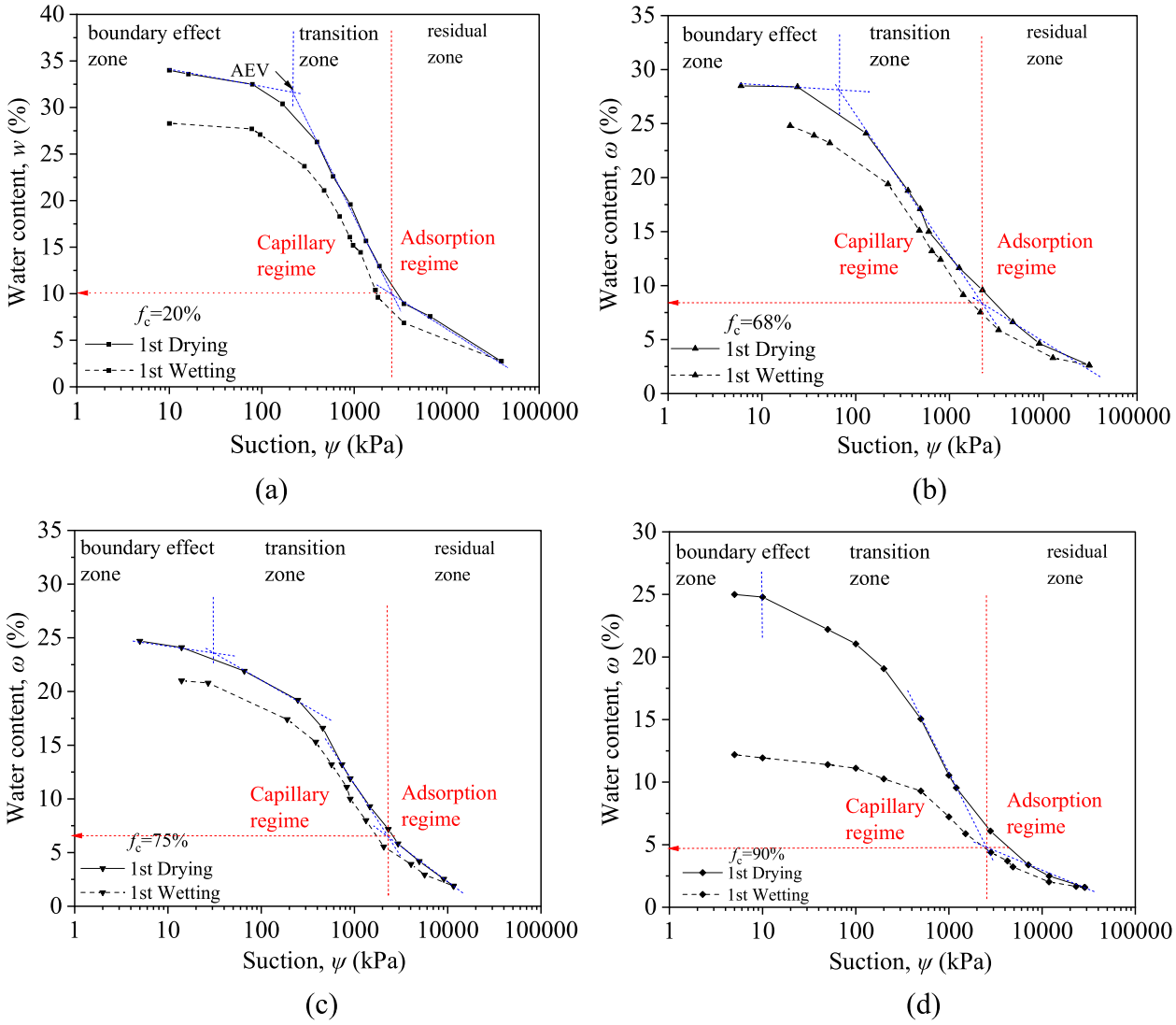

hibit consistent trends, which can be divided into three main zones: boundary effect zone, transition zone, and residual zone. The key points of the SWCC, including the AEV and residual suction, are determined using straight lines on a semi-log plot (Ng et al. 2024). As shown in Fig. 9, the first line is drawn horizontally at the saturated water content. The second line is tangent to the steepest part of the SWCC, while the third line passes through a high-suction reference point and extends back through the corresponding data points. In the boundary effect zone, the soil remains substantially saturated, and suction increases rapidly with only a slight reduction in water content. In the transition zone, more pronounced desaturation occurs with a significant reduction in the water content and a moderate increase in suction. The transition between the boundary effect zone and the transition zone corresponds to the AEV. Finally, in the residual zone, a further increase in suction results in minimal changes in water content, reflecting the soil residual saturation.

Table 1 reports the water content in correspondence of the AEV and at the beginning of the residual zone identified graphically from the drying paths as shown in Fig. 9. The data reported in Table 1 show a very good correspondence between the threshold water content separating the capillary and adsorption regimes from NMR analyses and the water content at the beginning of the residual zone identified from the retention curves. These results support the interpretation of water retention mechanisms by Lu and Dong (2017) and Lu (2019). In the capillary regime, the SWCC strongly depends on the pore-size distribution. As shown in Table 1, increasing coarse content leads to a decrease in the water content at AEV, from 32% ($\psi = 220$ kPa) to 22% ($\psi = 10$ kPa) for $f_c = 20\%$ and $f_c = 90\%$, respectively. Additionally, the amount of adsorbed water directly relates to the fine content. As the coarse content increases from 20% to 90%, the water content marking the onset of the adsorption regime decreases from 10% to 5%. The residual matric suction of soils with different coarse contents is similar, approximately 2–3 MPa. In the residual zone, water retention is controlled by interaggregate pores within clay aggregates, which are relatively unaffected by changes in coarse content. The adsorption forces at this

Fig. 10. Soil shrinkage curves under first drying and wetting cycle: (*a*) $f_c = 20\%$; (*b*) $f_c = 68\%$; (*c*) $f_c = 75\%$; and (*d*) $f_c = 90\%$.

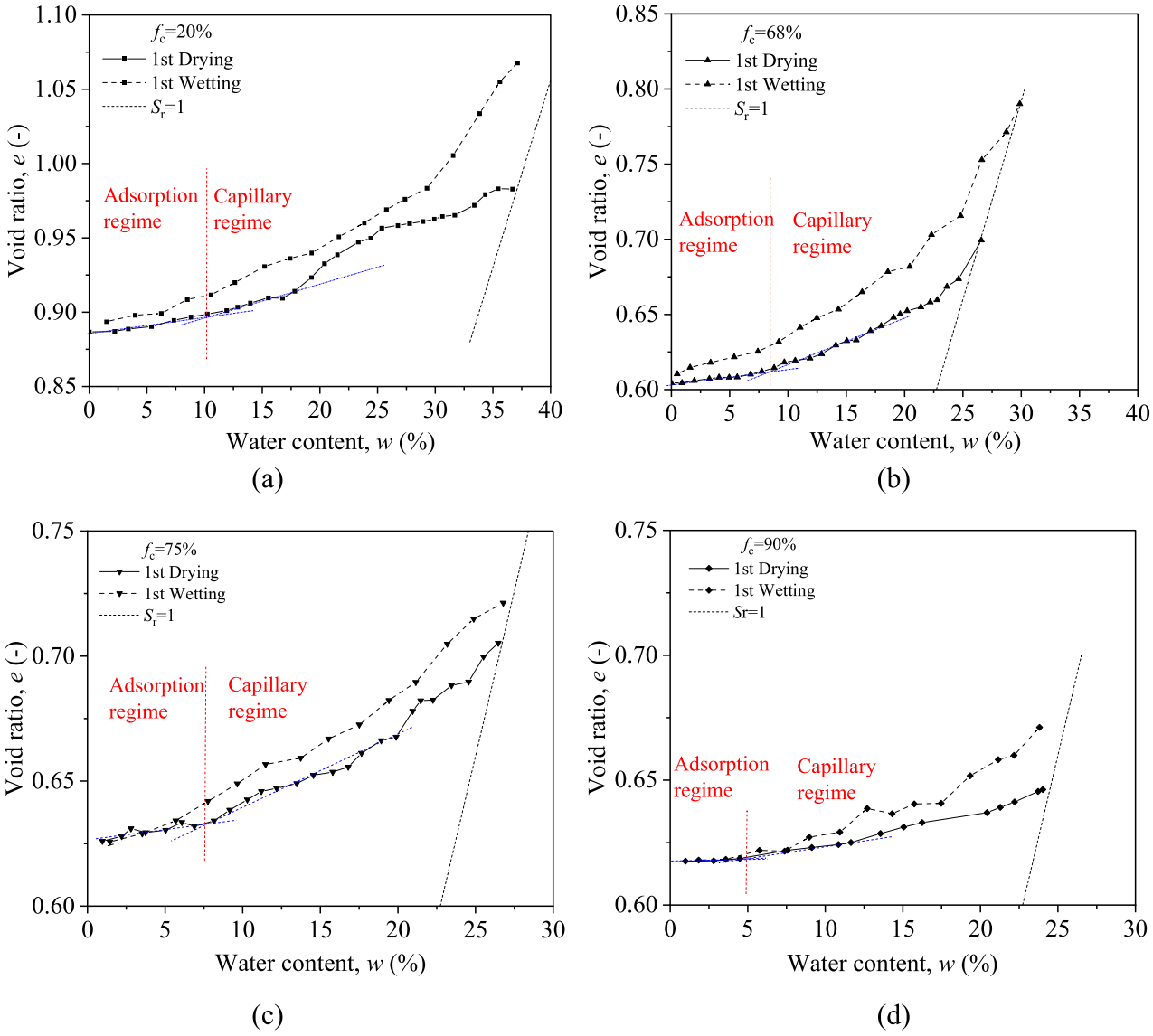

stage are dictated by the clay aggregate properties rather than the overall grain structure of the mixture, as illustrated in Fig. 8. This aligns with Su et al. (2022), who found that in the high-suction range, SWCC remains independent of the coarse fraction, as water retention is dominated by adsorption within fine soil aggregates.

As described by Ng et al. (2016), key features of the SWCC, including the AEV, inflection points, and curve shape, can be interpreted using the corresponding pore size distribution. As shown in Fig. 5, with increasing coarse content, an additional T_2 signal appears in the 100–1000 ms range. However, this second sigmoid function is less pronounced than the first, resulting in an overall single sigmoid SWCC. Specifically, for $f_c = 90\%$, the most significant hysteresis occurs at 5–20 kPa suction, corresponding to its AEV. This phenomenon is likely attributed to the presence of constricted large pores (Fig. 4*b*), which are only accessible through smaller pores.

Volume change during drying and wetting processes

Figure 10 displays the SSCs for samples with different coarse contents, $f_c = 20\%$, $f_c = 68\%$, $f_c = 75\%$, and $f_c = 90\%$, in terms of void ratio and water content upon first drying–wetting paths. The dashed line represents fully saturated conditions with soil volume change equal to water volume change. It is worth noticing that despite the soil samples being compacted to a target equal initial void ratio, 0.62, during saturation the samples swelled. The higher swelling was registered for soils with lower coarse content. The initial void ratio at the beginning of the shrinkage tests was 0.98, 0.68, 0.71, and 0.64 (Fig. 10).

Following the proposal by Lu and Dong (2017), the shrinkage curve is graphically divided into two regimes, capillarity and adsorption. As shown in Fig. 10, the boundary between the two regimes is identified by the intersection points of the tangent lines. The water content at these transition

Fig. 11. Hysteretic of soils with $f_c = 20\%$, $f_c = 75\%$, and $f_c = 90\%$. (*a*) Soil water characteristic curve and (*b*) degree of hysteresis (D_h).

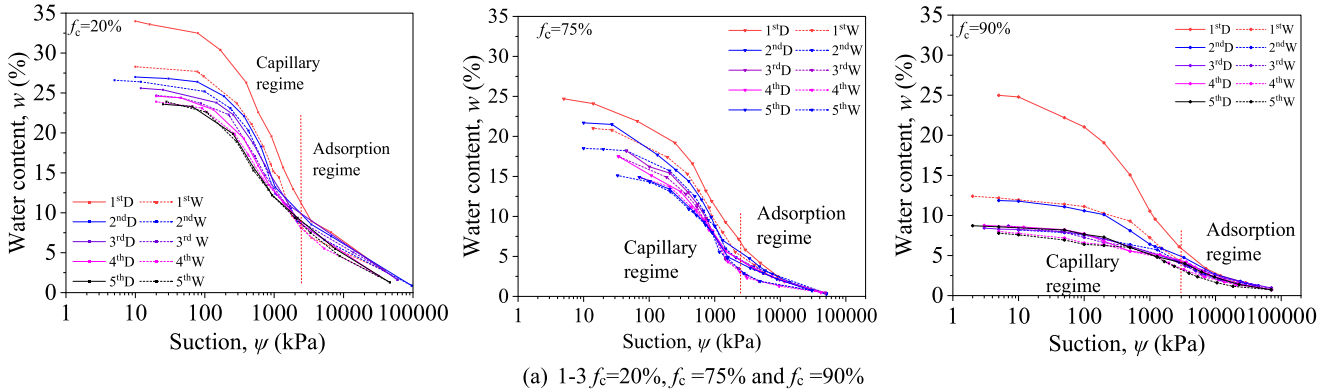

(a) 1-3 f_c=20%, f_c =75% and f_c =90%

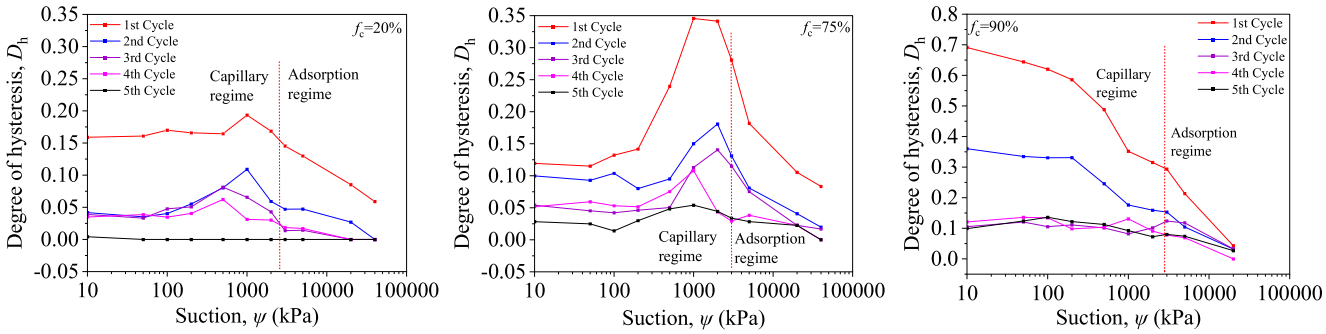

(b) 1-3 f_c=20%, f_c =75% and f_c =90%

points, as reported in Table 1, is generally consistent with both the NMR and the SWCC thus further confirming that mechanisms of capillarity and adsorption controlling moisture migration across the different tests.

As shown in Fig. 10, the vast majority of the overall soil volume change takes place in the capillary regime as a result of capillary forces at the curved air–water interface acting as normal stresses on the particle surfaces thus pulling the particles together. In fine-controlled soil with $f_c = 20\%$, the volume change during drying in the capillary regime (from $e = 0.98$ to 0.89) accounts for nearly 86% of the total volume change. As the coarse content increases, the proportion rises. Specifically, for f_c values of 68%, 75%, and 90%, the volumetric changes in the capillary regime account for 89%, 93%, and 97% of the total volume change, respectively. In the adsorption regime, moisture migration primarily occurs within clay aggregates, leading to minimal volume change depending on the coarse content as shown in the last portion of the SSC in Fig. 10.

Hysteresis in water migration and volume change

Figure 11*a* presents the evolution of the retention curves for specimens with $f_c = 20\%$, 75%, and 90% over five drying and wetting cycles. As shown in Fig. 11*a*, the SWCC of various soil types exhibits a significant hysteresis effect. When comparing the drying and wetting curves within a single cycle, the wetting curve is consistently positioned below the drying curve indicating a reduction in the retention capacity. The hydraulic hysteresis of SWCC was quantified according to the methodology proposed by Lu and Korshidi (2015). The step-wise hysteresis at a desired suction is defined as the difference between wetting and drying water content over the mean water content according to eq. 2. The average hysteresis over the whole range of suction considered can be expressed according to eq. 3.

$$(2) \quad D_{hi} = \frac{w_{di} - w_{wi}}{w_{mi}}$$

$$(3) \quad D_h = \frac{\sum_{i=j}^{i=k} \frac{w_{di} - w_{wi}}{w_{mi}}}{k - j + 1}$$

where D_{hi} is the degree of hysteresis at the ith suction level, w_{di} is the corresponding water content on the drying path, w_{wi} is the corresponding water content on the wetting path, and w_{mi} is the average water between the two drying and wetting paths.

Figure 11*b* illustrates the degree of hysteresis against suction for specimens with $f_c = 20\%$, 75%, and 90% over five drying and wetting cycles. Across all specimens, hysteresis is more pronounced in the capillary regime than in the adsorption region. In the capillary-dominant region, the combined effects of ink-bottle pores, contact angle variation, and entrapped air significantly influence retention behavior along the wetting and drying paths, resulting in pronounced hydraulic hysteresis. In the adsorption region, as described by Lu and Korshidi (2015), the intermolecular attractive forces

Fig. 12. Hysteretic of soils with $f_c = 20\%$, $f_c = 75\%$, and $f_c = 90\%$. (*a*) Soil shrinkage curves (SSCs) and (*b*) T_{dom}.

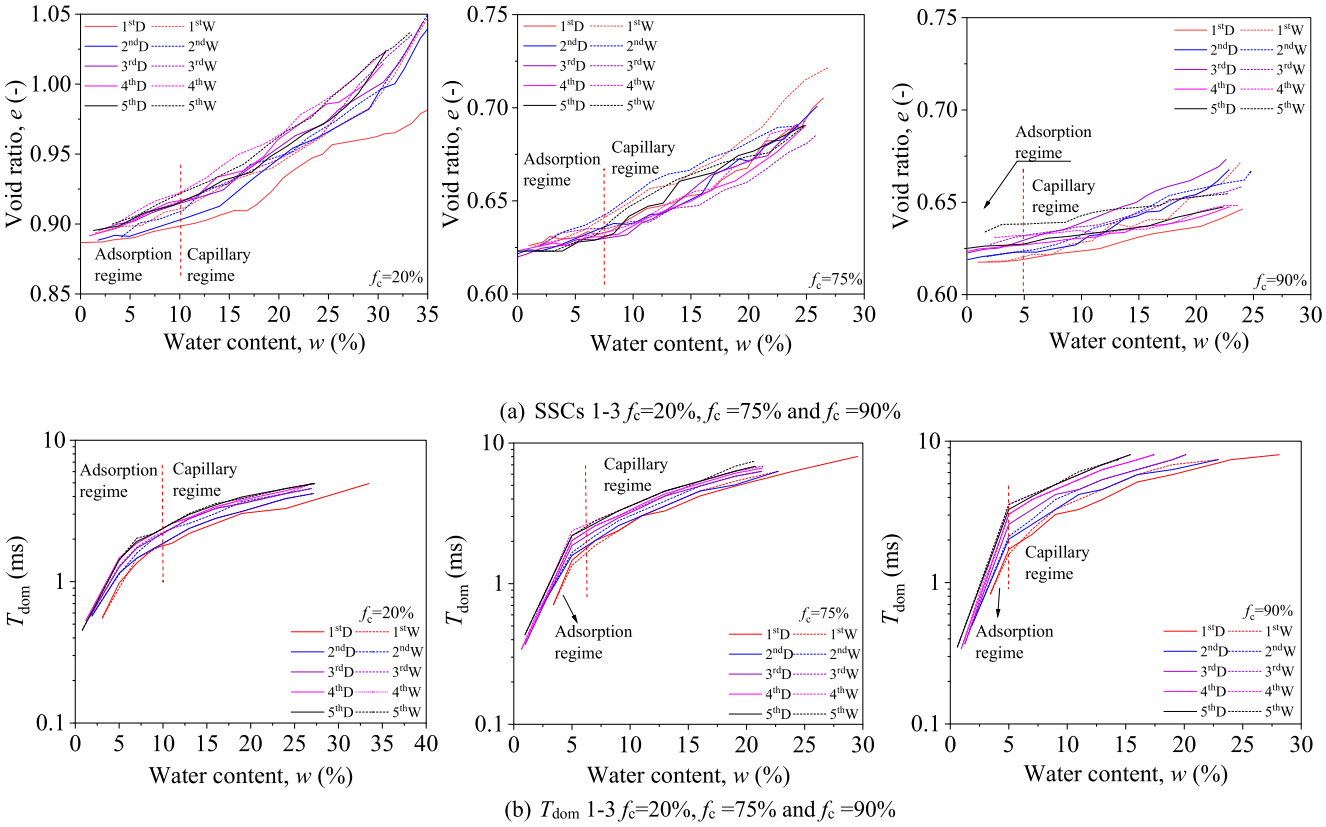

(a) SSCs 1-3 f_c=20%, f_c =75% and f_c =90%

(b) T_{dom} 1-3 f_c=20%, f_c =75% and f_c =90%

between oxygen/hydroxyl anions and hydrogen cations govern the hydration mechanism in nonexpandable minerals like kaolinite, leading to minimal hydraulic hysteresis. Since kaolin is the primary mineral in the fines of the tested soil, the degree of hysteresis decreases in the high suction range.

The conceptual hysteresis model proposed by Hillel (1998), based on the analogy of an ink bottle, explains hydraulic hysteresis as being more pronounced with increased nonuniformity in pore size distribution (Sadeghi et al. 2024). As shown in Figs. 3 and 4, small intra-aggregate pores dominate the pore structure for $f_c = 20\%$, while both intra-aggregate and inter-aggregate pores are significant for $f_c = 75\%$, and larger inter-aggregate pores dominate for $f_c = 90\%$, influencing the SWCC primarily in the very low suction range. According to Fig. 11*b*, hydraulic hysteresis during the first drying–wetting cycle increases with rising coarse content, with the average degree of hysteresis in the capillary range being 0.17, 0.27, and 0.56 for $f_c = 20\%$, $f_c = 75\%$, and $f_c = 90\%$, respectively.

The magnitude of hysteresis gradually decreases with the number of drying–wetting cycles. For $f_c = 20\%$, the average degree of hysteresis in the capillary range decreases from 0.17 to 0.06, 0.05, 0.04, and 0.0006 over successive cycles. For $f_c = 75\%$, it decreases from 0.25 to 0.11, 0.07, 0.06, and 0.04, and for $f_c = 90\%$, it decreases from 0.56 to 0.30, 0.11, 0.096, and 0.11. This reduction is likely due to the stabilization of the pore structure and entrapped air after repeated cycles. The results from the SWCC in Fig. 11*a* confirm this tendency, showing that as the number of cycles increases, the volume differences between the drying and wetting paths gradually diminish, and the curves converge, indicating increasing soil structure stability. This effect is particularly significant in the capillary regime, where most of the volume changes occur.

Figure 12 presents the shrinkage curves and the T_{dom} from NMR analyses for specimens with $f_c = 20\%$, 75%, and 90% over five drying and wetting cycles. Notably, during the first drying–wetting cycle, the wetting process caused significant volume expansion, primarily due to the experimental setup. Specifically, before the initial drying, samples were saturated under constrained conditions. However, after the first drying, the wetting process was conducted under unconfined conditions. All subsequent drying–wetting cycles were also performed under unconfined conditions. As shown in Fig. 12*b*, the results for T_{dom} are consistent with the SWCC, indicating that the water retention capacity of the soil gradually decreases with each drying–wetting cycle. Consequently, for the same water content, the T_2 value during the wetting process is greater than that during drying, suggesting that pore water in the wetting process occupies larger pores to maintain the same moisture. As a result, the T_{dom} curve under the wetting process consistently lies above that of the drying process. As the drying–wetting cycles continue, the T_2 curve shifts upward. However, with an increasing number of cycles, the magnitude of this shift gradually diminishes, reflecting a progressive reduction in the hysteresis effect.

For all three different coarse fractions, the hysteresis is much more pronounced in the capillary regime than in the adsorption regime. The difference arises from distinct water movement mechanisms in these two regions, as illustrated in

Figs. 3 and 4. In the capillary regime, larger inter-aggregate pores primarily hold water, with the shape and size of these pores influencing water flow and causing noticeable hysteresis. Significant volume changes in this region further amplify the hysteresis effect. In contrast, the adsorption regime involves soil particles absorbing water as bound water on their surfaces. Here, water movement depends mainly on particle surface hydration and crystalline cation hydration. Additionally, minimal changes in volume and pore structure in the adsorption region lead to weaker hysteretic effects.

Conclusions

Comprehensive laboratory tests were conducted on widely graded coarse soils to investigate pore water migration and deformation under multiple wetting and drying cycles. NMR tests, soil shrinkage tests, and soil water retention tests were performed on five types of soil with varying coarse contents. Five drying–wetting cycles were executed to examine the hysteretic behaviour. Additionally, SEM analyses were conducted to assess changes in soil fabric during the drying and wetting processes. Based on the experimental results, the following conclusions can be drawn:

(1) Widely graded coarse soils are characterised by inter-aggregate and intra-aggregate pores. Inter-aggregate pores are located between clay aggregates, while intra-aggregate pores exist within the clay aggregates, where water is adsorbed onto particle surfaces or within the lattice of clay particles. During drying–wetting cycles, the expulsion and absorption of water in both pore types are influenced by capillary and adsorption forces, respectively.
(2) In the capillary regime, inter-aggregate pore water drains quickly during drying, creating capillary forces at the curved air–water interface within these pores. These forces generate normal stresses that pull particles closer, resulting in substantial volume changes and a denser soil structure. The hysteresis observed in SWCC, SSC, and T_{dom} is particularly pronounced in this regime, as it is influenced by the distribution of inter-aggregate pores and is further amplified by significant volume changes. In the adsorption regime, intra-aggregate pore water is gradually drained from the clay aggregates, causing the crystal platelets to compact and resulting in the shrinkage of the clay aggregates. As a result, the morphology of the clay aggregates becomes more pronounced, while the overall deformation of the soil skeleton is relatively minimal at this stage. The hysteresis effect, primarily influenced by particle surface hydration, is less pronounced.
(3) As the coarse content increases, the water content corresponding to the transition point between the capillary regime and the adsorption regime decreases. Soils with a higher fine content are more sensitive to water exchange, exhibiting greater volume changes, particularly in the adsorption regime where the volume change is more pronounced.

The experimental results in this study offer valuable insights into the engineering behaviour of widely graded coarse soils under changing moisture conditions, which is especially important for geotechnical applications in areas with cyclic wetting and drying. The observed hysteresis in soil water retention and shrinkage highlights the importance of considering water migration in soil-based structural designs and carefully selecting soil gradation for engineering projects. To fully understand the long-term performance of earth structures under these cycles, further research is needed to explore the impact of water migration on soil compressibility, shear strength, and cracking.

Article information

History dates

Received: 1 November 2024
Accepted: 28 February 2025
Accepted manuscript online: 4 March 2025
Version of record online: 8 April 2025

Copyright

Data availability

Some or all data, models, or code generated or used during the study are available from the corresponding author upon reasonable request.

Author information

Author ORCIDs

Hongfen Zhao https://orcid.org/0000-0002-5099-0837
Stefano Muraro https://orcid.org/0000-0003-0737-9378
Xu Li https://orcid.org/0000-0002-0133-0795

Author contributions

Conceptualization: HZ
Data curation: JL, QX
Formal analysis: JL
Funding acquisition: HZ
Methodology: HZ, JL, SM, XL
Supervision: HZ
Validation: HZ
Visualization: JL
Writing – original draft: HZ, JL
Writing – review & editing: HZ, SM, XL

Competing interests

The authors declare there are no competing interests.

Funding information

This work was founded by the National Natural Science Foundation of China (No. 52279121; 52025094), Guangdong Basic and Applied Joint Funding for Offshore Wind Power (No. 2023A1515240069) and Science and Technology Innovation Program from Water Resources of Guangdong Province (2024-05).

References

ASTM. 2020. Standard practice for classification of soils for engineering purposes (unified soil classification system). D2487, West Conshohocken, PA.

Burton, G.J., Pineda, J.A., Sheng, D.C., and Airey, D. 2015. Microstructural changes of an undisturbed, reconstituted and compacted high plasticity clay subjected to wetting and drying. Engineering Geology, **193**: 363–373. doi:10.1016/j.enggeo.2015.05.010.

Chen, P., and Lu, N. 2018. Generalized equation for soil shrinkage curve. Journal of Geotechnical and Geoenvironmental Engineering, **144**(8): 04018046. doi:10.1061/(ASCE)GT.1943-5606.0001889.

Farulla, C.A., Ferrari, A., and Romero, E. 2010. Volume change behaviour of a compacted scaly clay during cyclic suction changes. Canadian Geotechnical Journal, **47**(6): 688–703. doi:10.1139/T09-138.

Fredlund, D.G. 2019. State of practice for use of the soil-water characteristic curve (SWCC) in geotechnical engineering. Canadian Geotechnical Journal, **56**(8): 1059–1069. doi:10.1139/cgj-2018-0434.

Frydman, S., and Baker, R. 2009. Theoretical soil-water characteristic curves based on adsorption, cavitation, and a double porosity model. International Journal of Geomechanics, **9**(6): 250–257. doi:10.1061/(ASCE)1532-3641(2009)9:6(250).

Hillel, D. 1998. Environmental soil physics: fundamentals, applications, and environmental considerations. Elsevier.

Kong, L., Sayem, H.M., and Tian, H. 2018. Influence of drying–wetting cycles on soil-water characteristic curve of undisturbed granite residual soils and microstructure mechanism by nuclear magnetic resonance (NMR) spin-spin relaxation time (T_2) relaxometry. Canadian Geotechnical Journal, **55**(2): 208–216. doi:10.1139/cgj-2016-0614.

Leong, E.C., and Wijaya, M. 2015. Universal soil shrinkage curve equation. Geoderma, **237–238**: 78–87. doi:10.1016/j.geoderma.2014.08.012.

Li, X. 2023. Soil mechanics laboratory manual. Tsinghua University Press and Beijing Jiaotong University Press.

Li, X., and Zhang, L.M. 2009. Characterization of dual-structure pore-size distribution of soil. Canadian Geotechnical Journal, **46**(2): 129–141. doi:10.1139/T08-110.

Liu, H.Y., Nagula, S., Jostad, H.P., Piciullo, L., and Nadim, F. 2024. Considerations for using critical state soil mechanics based constitutive models for capturing static liquefaction failure of tailings dam. Computers and Geotechnics, **167**: 106089. doi:10.1016/j.compgeo.2024.106089.

Lu, N. 2019. Linking soil water adsorption to geotechnical engineering properties. *In* Geotechnical fundamentals for addressing new world challenges. *Edited by* N. Lu and J.K. Mitchell. Springer Series in Geomechanics and Geoengineering. doi:10.1007/978-3-030-06249-1-4.

Lu, N., and Dong, Y. 2017. Correlation between soil-shrinkage curve and water-retention characteristics. Journal of Geotechnical and Geoenvironmental Engineering, **143**(9): 04017054. doi:10.1061/(ASCE)GT.1943-5606.0001741.

Lu, N., and Khorshidi, M. 2015. Mechanisms for soil-water retention and hysteresis at high suction range. Journal of Geotechnical and Geoenvironmental Engineering, **141**(8): 04015032. doi:10.1061/(ASCE)GT.1943-5606.000132.

Ma, T., Wei, C., Yao, C., and Yi, P. 2020. Microstructural evolution of expansive clay during drying–wetting cycle. Acta Geotechnica, **15**(8): 2355–2366. doi:10.1007/s11440-020-00938-4.

Mu, Q.Y., Dong, H., Liao, H.J., Zhou, C., Li, S.B., and Zhang, J.W. 2022. Effects of in situ wetting–drying cycles on the mechanical behaviour of an intact loess. Canadian Geotechnical Journal, **59**(7): 1281–1284. doi:10.1139/cgj-2020-0696.

Ng, C.W.W., and Pang, Y.W. 2000a. Experimental investigations of the soil-water characteristics of a volcanic soil. Canadian Geotechnical Journal, **37**: 1252–1264. doi:10.1139/t00-056.

Ng, C.W.W., and Pang, Y.W. 2000b. Influence of stress state on soil-water characteristics and slope stability. Journal of Geotechnical and Geoenvironmental Engineering, **126**(2): 157–166. doi:10.1061/(ASCE)1090-0241(2000)126:2(157).

Ng, C.W.W., Sadeghi, H., Hossen, S.B., Chiu, C.F., Alonso, E.E., and Baghbanrezvan, S. 2016. Water retention and volumetric characteristics of intact and re-compacted loess. Canadian Geotechnical Journal, **53**(8): 1258–1269. doi:10.1139/cgj-2015-0364.

Ng, C.W.W., Zhou, C., and Ni, J.J. 2024. Advanced unsaturated soil mechanics: theory and applications. CRC Press.

Nitao, J.J., and Bear, J. 1996. Potentials and their role in transport in porous media. Water Resources Research, **32**(2): 225–250. doi:10.1029/95WR02715.

Oualmakran, M., Mercatoris, B.C.N., and François, B. 2016. Pore-size distribution of a compacted silty soil after compaction, saturation, and loading. Canadian Geotechnical Journal, **53**(12): 1902–1909. doi:10.1139/cgj-2016-0184.

Peng, X., and Horn, R. 2013. Identifying six types of soil shrinkage curves from a large set of experimental data. Soil Science Society of America Journal, **77**(2): 372–381. doi:10.2136/sssaj2011.0422.

Romero, E., and Simms, P.H. 2008. Microstructure Investigation in unsaturated soils: a review with special attention to contribution of mercury intrusion porosimetry and environmental scanning electron microscopy. Geotechnical and Geological Engineering, **26**(6): 705–727. doi:10.1007/s10706-008-9204-5.

Sadeghi, H., Heydari, A., and Zhou, C. 2024. Insights into the fluid retention and shrinkage of a lean clay under the combined influence of microstructure, solute concentration and salt species. Acta Geotechnica, 1–18. doi:10.1007/s11440-023-02206-7.

Su, Y., Cui, Y.J., Dupla, J.-C., and Canou, J. 2022. Soil-water retention behaviour of fine/coarse soil mixture with varying coarse grain contents and fine soil dry densities. Canadian Geotechnical Journal, **59**: 291–299. doi:10.1139/cgj-2021-0054.

Sun, W.J., and Cui, Y.J. 2017. Investigating the microstructure changes for silty soil during drying. Géotechnique, **68**(11): 370–373. doi:10.1680/jgeot.16.P.165.

Tang, C.S., Cheng, Q., Gong, X., Shi, B., and Inyang, H.I. 2023. Investigation on microstructure evolution of clayey soils: a review focusing on wetting/drying process. Journal of Rock Mechanics and Geotechnical Engineering, **15**(1): 269–284. doi:10.1016/j.jrmge.2022.02.004.

Tian, H., Wei, C., Wei, H., Yan, R., and Chen, P. 2014. An NMR-based analysis of soil–water characteristics. Applied Magnetic Resonance, **45**(1): 49–61. doi:10.1007/s00723-013-0496-0.

Tuller, M., Or, D., and Dudley, L.M. 1999. Adsorption and capillary condensation in porous media: liquid retention and interfacial configurations in angular pores. Water Resources Research, **35**(7): 1949–1964. doi:10.1029/1999WR900098.

Wang, D.Y., Zeng, Q.J., Wang, J., and Zhou, M. 2020. Effect of dry-wet cycle on stability of granite residual soil slope. IOP Conference Series: Earth and Environmental Science, **526**(1): 012046. doi:10.1088/1755-1315/526/1/012046.

Wen, T., Wang, P., Shao, L., and Guo, X. 2021. Experimental investigations of soil shrinkage characteristics and their effects on the soil water characteristic curve. Engineering Geology, **284**: 106035. doi:10.1016/j.enggeo.2021.106035.

Zhang, Y., Yang, G., Chen, W., and Sun, L. 2022. Relation between microstructures and macroscopic mechanical properties of earthen-site soils. Materials, **15**(17): 6124. doi:10.3390/ma15176124.

Zhao, H. 2023. The effect of soil fabric on shrinkage behaviour and microstructure evolution of soft soils upon drying. Canadian Geotechnical Journal, **60**(4): 438–452. doi:10.1139/cgj-2021-0421.

Zhao, H.F., Zhang, L.M., and Chang, D.S. 2013a. Behavior of coarse widely graded soils under low confining pressures. Journal of Geotechnical and Geoenvironmental Engineering, **139**(1): 35–48. doi:10.1061/(ASCE)GT.1943-5606.0000755.

Zhao, H.F., Zhang, L.M., and Fredlund, D.G. 2013b. Bimodal shear-strength behavior of unsaturated coarse-grained soils. Journal of Geotechnical and Geoenvironmental Engineering, **139**(12): 2070–2081. doi:10.1061/(ASCE)GT.1943-5606.0000937.

Zhao, Y. 2022. The influence of rainfall and evaporization wetting-drying cycles on the slope stability. Advances in Meteorology, **2022**: 1–8. doi:10.1155/2022/5775424.

Zhao, Y., Wu, L., and Li, X. 2024a. NMR-based pore water distribution characteristics of silty clay during the soil compaction, saturation, and drying processes. Journal of Hydrology, **636**: 131240. doi:10.1016/j.jhydrol.2024.131240.

Zhao, Y., Li, X., Wang, M., and Zheng, S.F. 2024b. Quantitative characterization of soil micropore structure and pore water content using nuclear magnetic resonance: challenges and calibration methods. Frontiers of Structural and Civil Engineering, In press. doi:10.1007/s11709-024-1137-4.